PAPER

Check for updates

Bioinspired scaffold design using a custom Voronoi path generator for extrusion-based 3D printing

Federico Farina,[a,b,c] Michela Licciardello,[a,b] Lorenzo Moroni, [ID][c] Joanna Babilotte,[c] Gianluca Ciardelli [ID][a,b,d] and Chiara Tonda-Turo [ID] *[a,b]

Natural systems are often arranged into specialized patterns, conferring unique biological features and functions to tissues and organs. Engineered microenvironments, aiming to support cell cultures and tissue-specific functions, have to accurately recreate biological arrangements for the development of relevant biological models. To this aim, we designed a custom Python-based software tool to produce the biomimetic and irregular structure known as the Voronoi pattern by extrusion-based additive manufacturing techniques—melt electrowriting (MEW) and fused deposition modelling (FDM). The printed Voronoi backbone was integrated with an electrospun nanofibrous membrane, providing a multiscale construct that combines the morphological fidelity of additive manufacturing with the ECM-like features of electrospinning. As the Voronoi arrangement is observed in lung tissue organization, we cultured alveolar epithelial and endothelial cells on the upper and lower sides of the construct, respectively, to reassemble the alveolar-capillary barrier *in vitro*. The culture was maintained under air–liquid-interface (ALI) conditions for 10 days, reaching complete coverage of the two sides of the construct and a physiological-like organization of the cells within the biomimetic architecture. Overall, this study introduces a flexible approach that merges digital design and hybrid fabrication to manufacture *in vitro* tissue models that more closely mimic physiological environments.

1 Introduction

Patterns are frequently observed in natural systems, across different biological contexts and at varying length scales. These arrangements result from evolutionary and adaptive processes[1,2] that lead to the emergence of optimized structures capable of supporting complex biological functions. To properly exploit this evolutionary optimization, biomimicry has become a key design feature in the tissue engineering field, particularly concerning tissue modelling.[3,4] By replicating morphological, topological and mechanical cues observed in the native target tissues, the biomimetic approach leads to the development of engineered microenvironments that accurately support cell cultures and tissue-specific functions.

Among the various spatial organizations possible to observe in nature, the Voronoi pattern stands out as a biologically rele-

vant geometry, capable of capturing the irregular but optimized arrangement of adjacent units within a confined space. Specifically, a Voronoi pattern divides a plane or a volume into heterogeneous regions based on the proximity to a set of points (conventionally named seeds), resulting in polygonal domains. This type of structural arrangement can be found in several biological systems,[5–9] including the organization of epithelial cells,[10–12] the lobular architecture of the liver,[13] and the porous structure of cancellous bone.[14–17]

Across its various applications, the Voronoi-like organization contributes to achieving efficient spatial occupation,[9] balanced surface-to-volume ratios, and effective mechanical load distributions,[15,18] outperforming more regular geometric and homogeneous designs. Due to these properties, the Voronoi pattern has been envisioned as a design principle in the development of bioinspired scaffolds for tissue engineering applications through additive manufacturing technologies.[14–17,19]

Some pioneering studies applied this design strategy to trabecular bone regeneration,[20–22] where Voronoi-based structures fabricated *via* additive manufacturing supported tissue ingrowth and vascularization both *in vitro* and *in vivo*. In these applications, such architectures demonstrated their suitability for replicating complex biological environments.

[a]Politecnico di Torino, Department of Mechanical and Aerospace Engineering, Torino, 10129, Italy. E-mail: chiara.tondaturo@polito.it
[b]Politecnico di Torino, Bioinside Lab, Torino, 10129, Italy
[c]MERLN Institute for Technology-Inspired Regenerative Medicine Department of Complex Tissue Engineering, Maastricht University, Maastricht 6229 ER, the Netherlands
[d]Biomedical Engineering Center, Kansai Medical University, Osaka, 5731010, Japan

Beyond bone tissue, Voronoi patterns have also been extensively adopted in computational studies of the geometry and mechanics of the alveolar structures.[23–26] However, their use in the fabrication of *in vitro* alveolar tissue models remains unexplored. Replicating the architecture of alveolar tissue is particularly challenging, as it combines a high degree of structural heterogeneity with an irregular spatial organization. Previous attempts to recreate alveolar-like environments have often relied on symmetrical geometries, such as regular hexagons or spherical cavities.[27,28] These approaches aim to reproduce the relative disposition of alveoli within the tissue but only partially reflect the actual physiological architecture. In this context, the Voronoi pattern offers a biomimetic representation of the alveolar geometry, closely resembling the natural formation of intralveolar septa between adjacent alveoli (Fig. 1a–b).

Here, a two-dimensional Voronoi layout was employed to design a nature-inspired alveolar array, providing a more biomimetic spatial representation of the native architecture, aimed at the development of a more physiologically relevant alveolar *in vitro* model. Two extrusion-based additive manufacturing techniques—melt electrowriting (MEW) and fused deposition modelling (FDM)—were selected for fabrication, as both have been widely employed in tissue engineering applications for the production of porous scaffolds with controlled architecture and mechanical properties.[31–38] The implementation of such a geometrically complex and non-repeating pattern presents significant technical challenges, particularly in generating a continuous extrusion path suitable for MEW and FDM. Standard slicing software is generally optimized for regular or parametric geometries and lacks the flexibility to manage topologically irregular structures such as Voronoi patterns.

While Voronoi pattern generators and Voronoi-based infill strategies are available in several commercial slicers (for example, Cura, PrusaSlicer), these tools do not allow the generation of a fully continuous, interruption-free extrusion path within a single layer. Current continuity-oriented features, such as spiral or "vase" modes, are designed to grant continuity along the *Z* direction between consecutive layers rather than in-plane continuity, which is a critical requirement for MEW and beneficial for FDM to optimize the path. As a result, existing software solutions are not suitable for generating controlled continuous toolpaths across complex Voronoi architectures, as needed for this application.

To overcome this limitation, a custom Python-based software tool was developed, with the aim of generating, analyzing, and converting the Voronoi layout into G-Code optimized for MEW and FDM printing. Finally, the printed Voronoi structure was combined with an electrospun nanofibrous mat that replicates the pulmonary basal membrane, as extensively used in the literature,[39–43] while allowing cell seeding confined within the Voronoi pattern. Such a combination is in line with several reported approaches that aim at merging additive and conventional techniques to benefit from advantages each method offers.[44–57] The resulting construct was then mounted on a transwell insert, enabling the coculture of epithelial and endothelial cells on the two opposite sides of the scaffold, mimicking the physiological interface observed in the native tissue.

2 Methods

2.1 Software overview

The *Voronoi Path Generator* (PyVoroGen) is a software system developed by the authors that aims at the generation of a path in G-Code suitable to replicate the Voronoi pattern with extrusion-based techniques, whose source code is publicly available on GitHub. This path is designed to manage the reproduction of this complex pattern with a continuous flow, necessary for the Melt Electrowriting (MEW) technique, and then adapted to be suitable for the Fused Deposition Modelling (FDM) technique. In addition to generating the path, this software analyzes the generated pattern according to the input parameters to provide theoretical information regarding the outcome of the 3D print.

The code was developed using Python 3 as the programming language and Visual Studio Code as the integrated development environment. Moreover, the FullControlXYZ library[58] was used to directly design a path suitable for 3D printing after defining the path using graph theory.

2.2 Software architecture

The software architecture is organized into four main modules, as illustrated in Fig. 2. Each module is dedicated to a specific step of the workflow that leads to the final output. Additionally, intermediate results are generated at each stage to enable graphical visualization and facilitate the evaluation
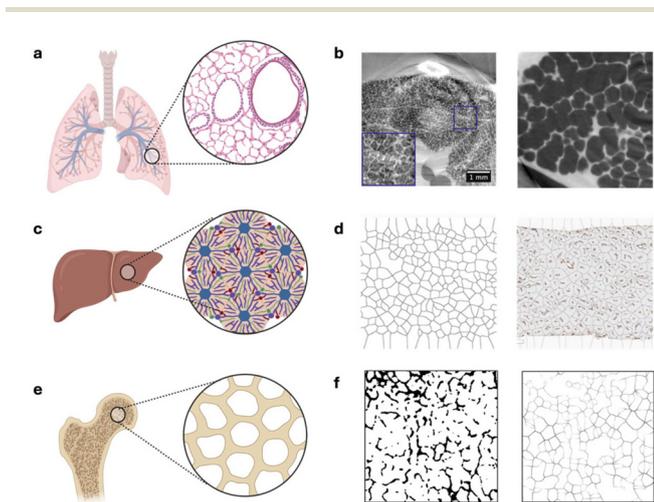

Fig. 1 Occurrence of Voronoi-like spatial optimization in native tissues. (a, c and e) Schematic illustrations of tissues and the corresponding organs, created with BioRender (https://BioRender.com). (b) Lung parenchyma, tomographic slices.[29] (d) Liver lobules: Voronoi-like diagram generated from the edges of individual lobules (left) and overlaid with immunostained histological sections (right).[13] (f) Cancellous bone tissue: binarized µCT scan (left) and images segmented using the Delaunay–Voronoi function in ImageJ (right).[30] Panels b, d and f are adapted with permission from the respective publications.
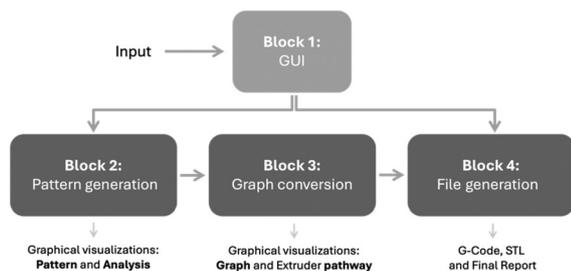
Fig. 2 Visualization of the main blocks of the software architecture.

of the corresponding outputs. An automatic folder system was implemented to better organize and facilitate the access to the output files. In particular, for each set of main input parameters defining the pattern, a dedicated folder is created to store both the graphical outputs and the key pattern features required for the computational workflow.

The entire process is started by running the main.py file, located in the main folder. Then, the user can interact only with the graphical user interface (GUI) to set the desired custom parameters and start the code workflow. Once the process is completed, the output files containing results are stored in the designated directories as previously described.

2.2.1 Block 1 – GUI. The first block of the architecture is dedicated to the GUI, where several inputs are set by the user, detailed as follows:

• Seed number: defines the number of seeds used to generate the pattern, with each seed acting as the generator of a Voronoi cell.

• Diameter of the pattern: sets the diameter (in millimeters) of the circular area occupied by the pattern.

• Fiber thickness: expected fiber diameter resulting from the printing process. This parameter is used in pattern analysis, extruder path visualization, and STL file generation.

• Center: defines the pattern's center position on the collector, customizable according to the coordinate system used by the user's printer.

• Border: a Boolean option to add a border around the pattern, facilitating manipulation of printed constructs, especially for small designs with thin fibers.

• Technique: allows the selection of one or both printing techniques (MEW and/or FDM), triggering the corresponding workflow.

• Conversion: enables the user to select the desired output format (STL and/or G-Code). If G-Code is selected, a secondary window prompts the user to set the main process parameters for G-Code generation.

Default values for each parameter are displayed in the corresponding GUI frames, which are defined and can be modified in the src/gui/config.py file. This block was developed using the *Tk-inter* library, providing an interactive and user-friendly interface for parameter selection.

2.2.2 Block 2 – pattern generation. The second block of the architecture is dedicated to the design of a Voronoi pattern with the parameters set by the user.

First, a custom function optimizes the spacing of a set of generating seeds between the points, while preserving their random distribution and ensuring minimal area variability in the corresponding cells of the final pattern. Briefly, the points are initially generated in polar coordinates and then filtered using a grid-based system and compartmentalized inside the diameter set in the GUI.

An additional set of generating seeds is placed along a circumference that surrounds the pattern. This step is necessary to constrain the pattern within the desired area, enhancing the disposition of the external segments.

After the optimization of the seed distribution, the pattern is generated using the scipy.spatial.Voronoi function. Finally, the segments that exceed the boundary set by the user are trimmed, and the Voronoi pattern vertices are updated for further processing.

To visualize this step of the process, the second block generates a graphical visualization of the seed distribution and the resulting Voronoi pattern, which is saved in the complementary files/images directory. Specifically, the "complementary files" folder is automatically created inside the main folder associated with the corresponding pattern, defined by the following two parameters: "Seeds number" and "Diameter of the pattern". The resulting folder name is formatted as follows: "Voronoi{*Seeds number*}s_{*Diameter of the pattern*} mm". Additionally, the "complementary files" folder stores the computed coordinates of the seeds, so that the same seed disposition is maintained during multiple executions of the program with the same values associated with "Seeds number" and "Diameter of the pattern".

An additional graphical output is produced by the second block, in order to enable area analysis of each cell of the pattern. This visualization consists of two different images: the first one displays the pattern with a colour-coded map corresponding to each cell's area, while the second illustrates a histogram of the cells' area distribution using the same colour code. The histogram additionally highlights the mean area value of the entire cell collection. Within this analysis, the "Fiber thickness" parameter affects the area calculation. Specifically, the area occupied by the fiber within each cell is subtracted, providing a more accurate estimation of the effective area in the physical print. This visualization is then saved in the same directory of the previous one.

2.2.3 Block 3 – graph conversion. The third block handles the conversion of the generated pattern into a graph, allowing the employment of graph theory algorithms to find a continuous path. Since the graph conversion process is a high computational cost process, the graph is saved in the complementary files directory. This stored version is reused in subsequent executions with the same parameters, following the same storage logic as the seed coordinates.

Specifically, the NetworkX function networkx.algorithms. euler.eulerian_circuit is used to return a closed continuous path that includes each edge of the graph, also known as the solution to the Chinese Postman Problem. Theoretically, the function should return a path where every edge is visited

exactly once. However, due to the non-Eulerian nature of the graph associated with a Voronoi pattern, the resulting path includes overlapping of segments in the sequence. This overlapping characteristic of the path does not raise concerns regarding the employment of MEW as a printing technique, since the distance between the extruder and the collector, along with the micrometric fiber diameter, does not affect the final outcome. In contrast, this characteristic does not comply with the technical specifications of the FDM technique. Therefore, a subsequent processing step is implemented to adapt the path for FDM printing. The function designed to solve this issue processes the path sequentially, stopping the extrusion and lifting the extruder whenever a segment is revisited, avoiding collision with the already printed filament while remaining on the same path.

The visualization of the outcomes of this block is divided into two main parts. Both the graph conversion and the continuous path along the Voronoi pattern are summarized in a graphical visualization stored in the complementary files/ images directory, following the same storage logic of the previous block. Additionally, the path is processed using the FullControlXYZ library to display the path in an interactive 3D environment in a separate window with the selected fiber thickness, which automatically opens during computation. A slight modification was made to the native FullControlXYZ function to be able to save the HTML file displaying the path, stored in the complementary files/images/fullcontrol directory.

2.2.4 Block 4 – file generation. Finally, the fourth block converts the generated path into two possible output formats, STL and G-Code, depending on the user's selection in the GUI, both with FullControlXYZ functions. The STL file specifically incorporates the fiber thickness parameter, providing an accurate 3D model of the printed output. The resulting files are then saved in the output directory, each in a dedicated subfolder named STL and gcodes, respectively.

Additionally, a PDF report is generated with the reportlab library to summarize the pattern parameters defined by the user and to collect the graphical outputs produced during computation, and is then saved in the same output directory, in the subfolder report.

2.3 Scaffold production

The scaffolds were produced using the G-Code obtained with the software previously described, with the number of seeds equal to 300 and a pattern diameter of 13.4 mm.

2.3.1 Melt electrowriting. Melt electrowritten scaffolds were printed with Novaspider v5 (CIC nanoGUNE, Spain) with a 0.4 mm nozzle, applying the voltage only onto the collector. To perform the printing, PCL (MW 42KDa, Polysciences) was employed, applying a pre-melting step of an hour at 100 °C to ensure the correct melting of the polymer before setting the temperature at 90 °C during the printing. A flow percentage of 10% was set on the screw system of the printer and a printing speed of 21 mm s^{-1} was used for printing. Due to the monolayer nature of the print, the nozzle height was maintained still at 5 mm at a voltage of 3.35 kV.

2.3.2 Fused deposition modelling. FDM prints were performed with a3D Bioplotter (Evisiontec), equipped with a 0.1 mm nozzle. PCL (MW 50 kDa, Polysciences) was used with a pre-melting step of two hours before printing at a temperature of 110 °C. During the printing, the temperature was maintained at the same value. A pressure of 0.9 bar was applied while using a printing speed of 0.1 mm s^{-1}.

2.3.3 Electrospinning. After the Voronoi-shaped backbones were manufactured with the previously described additive manufacturing techniques, electrospinning was performed directly on the construct surface, covering the top layer. The electrospun membrane was produced by following a previously defined protocol, optimized by Licciardello M. *et al.*[59] Briefly, a solution (15% w/v) was prepared by mixing PCL (MW 80 kDa, Sigma Aldrich, Italy) and gelatin (porcine skin, type A, Sigma Aldrich, Italy) in a ratio of 80 : 20 in a mixture of formic acid (Sigma Aldrich, Italy) and acetic acid (Fisher Scientific, Italy) at a 50 : 50 v/v ratio.

The solution was left under stirring for 24 hours; then, (3-glycidyloxypropyl) trimethoxysilane (GPTMS, Sigma Aldrich, Italy) was added at a concentration of 3.68% v/v to promote gelatin (Gel) crosslinking, as previously reported.[60]

Afterwards, the solution was loaded in a 5 ml syringe connected to a 21-G needle, and the electrospinning process to obtain randomly oriented fibers was conducted with the Novaspider v5 (CIC nanoGUNE, Spain) using a vertical configuration with a distance of 12 cm between the needle and a plane collector where the Voronoi-shaped backbones were previously placed. A voltage of 20 kV was set with a flow rate of 500 μL h^{-1}.

2.3.4 Software process validation. To assess the software's ability to predict scaffold pore size, theoretical predictions were compared with measurements from printed scaffolds. The comparison was performed in two steps: first, the physical porosity and the mean fiber diameter were evaluated through analysis of confocal images (acquired with an Eclipse Ti2 Nikon confocal microscope) using Fiji (ImageJ2); second, the experimentally measured mean fiber diameter of the scaffolds was used as input to generate the software's pore-size predictions. In particular, the porosity value was measured through the "Analyze Particles" function after thresholding aimed at increasing the contrast, necessary to clearly distinguish the scaffold porosities from the printed structure.

Three constructs per fabrication technique were evaluated. Since each scaffold was individually validated by comparing it with its corresponding software prediction, results were not averaged across replicates.

2.4 Cell culture

Human alveolar basal epithelial (A549) cells were obtained from ATCC and cultured in Roswell Park Memorial Institute 1640 (RPMI, Gibco, Life Technologies, Italy) medium supplemented with 10% fetal bovine serum (FBS, Gibco, Life Technologies, Italy), 1% L-glutamine (L-Glu, Gibco, Life Technologies, Italy) and 1% penicillin/streptomycin (P/S,

Gibco, Life Technologies, Italy). Human umbilical vein endothelial cells (HUVECs) were purchased from Innoprot (Spain) and subsequently expanded using a coating of rat tail collagen type I (Corning, Sigma Aldrich, Italy) in Endothelial Cell Medium (Innoprot, Spain).

2.4.1 Co-culture on the produced scaffolds. To perform the cell culture, the scaffolds were mounted on 12-well transwell inserts (CellQART®, SABEU GmbH and Co. KG, Germany) after removing the commercial membrane. Three different conditions were tested:

• FDM-produced scaffold (the electrospun top layer on the apical side).

• MEW-produced scaffold (the electrospun top layer on the apical side).

• PCL-Gel electrospun membranes mounted on transwell inserts following the protocol developed by Licciardello *et al.*[43] as a control.

The scaffolds were submerged in a 2% antibiotic–antimycotic solution and maintained at room temperature overnight. After rinsing with sterile phosphate-buffered saline (PBS, Gibco, Life Technologies, Italy), the scaffolds were sterilized with UV light for 1 hour, 30 minutes for each side of the patterned membrane. The mounted scaffolds were then functionalized by incubating in FBS at 37 °C overnight. A549 cells were suspended in 500 µL of cell culture medium and seeded at a density of 140 000 cells per cm^2 on the apical side of each membrane, maintaining a liquid–liquid interface culture until day 3. Then, an air–liquid interface (ALI) culture was established by removing the culture medium from the apical side of each transwell-based system until the end of the culture.

On day 7, HUVECs were pelleted and suspended in 30 µL of cell culture medium and seeded at a density of 100 000 cells per cm^2 by pipetting 3 single drops of 10 µL evenly on the surface. HUVECs were seeded on the basolateral side of the constructs, performed by flipping the transwell systems and directly pipetting on the scaffolds; the constructs were incubated upside down at 37 °C for 3 hours, then returned to their upright configuration to continue the cell culture in the normal configuration until day 10.

2.4.2 Immunostaining. To validate the cell culture, both fluorescence and immunofluorescence staining were performed at the end of the culture. On day 10, the constructs were rinsed with PBS and then fixed with 4% PFA. After fixing, samples were permeabilized using 0.2% v/v Triton X-100 in PBS for 10 min at RT, followed by a blocking step in 2% v/v BSA solution in PBS for 1 h at RT.

Samples were incubated with primary antibodies diluted in PBS with 1% v/v BSA and 0.1% v/v Tween 20. Immunostaining was conducted by dividing the constructs into two groups: one incubated with VE-cadherin (F-8) (Santa Cruz Biotechnology, 1 : 50, mouse) to stain the endothelial cells, and the other with E-cadherin (HECD-1) (Invitrogen, 1 : 2000, mouse) to target the epithelial cells.

The following day, the samples were washed with PBS with 1% v/v BSA and 0.1% v/v Tween 20 and incubated for 1 h at RT with secondary antibodies diluted in the same solution.

Cyan5 goat anti-mouse IgG (Invitrogen, 1 : 1000) was used to detect VE-cadherin and E-cadherin.

After further washing the samples in PBS with 1% v/v BSA and 0.1% v/v Tween 20, they were stained with FITC-phalloidin (1 : 60 dilution in 1% v/v BSA in PBS) to label the cytoskeleton, followed by a wash in PBS only and a final incubation with DAPI (Invitrogen, 1 : 5000) to stain the nuclei.

2.4.3 SEM analysis. The morphology of the complete scaffold and the integration of the electrospun membrane within the Voronoi backbone were assessed by scanning electron microscopy (SEM, Tescan Vega). Prior to imaging, the samples were coated with a thin layer of gold using a magnetron ion sputtering coater (SD-900, VPI).

2.4.4 Statistical analysis. All cell culture experiments were performed in triplicate, and results were reported as one representative image of each condition. For the software performance evaluation in predicting scaffold porosity, three different constructs per fabrication technique were analyzed. However, due to the nature of the validation procedure where each scaffold was independently compared with its corresponding software prediction, it was not possible to average the results across replicates.

3 Results and discussion

3.1 Software

The graphical user interface (GUI) was developed to avoid direct interaction with the code and is illustrated in Fig. 3. After launching the program, the main window appears (Fig. 3a), allowing users to input custom parameters. By default, a set of predefined values is displayed in the corresponding fields and can be modified by clicking directly on each input frame. Below the numerical inputs, a series of checkboxes enables the selection of additional options required to complete the input set and define the desired output for pattern generation. If the G-Code conversion option is enabled, a secondary window opens on the side (Fig. 3b) to input the relevant G-Code parameters. The generation process starts when the Generate button is pressed. A message then appears in the lower part of the window (Fig. 3c) displaying "Generating files, please wait...", confirming that the computation is in progress. Once completed, the generated path is shown in an interactive window. If both fabrication techniques are selected, the corresponding paths are displayed in separate preview windows, as illustrated in Fig. 3d. A final dialog box informs the user that the process has ended, and by clicking "OK", all open windows are closed. Alternatively, the user can simply close the dialog box, adjust the parameters, and repeat the generation process.

Following the parameter configuration by the user through the GUI, the software computes and displays a series of graphical visualizations related to the generated pattern.

The first output (Fig. 4a) illustrates the distribution of the seeds and the corresponding Voronoi layout. Specifically, the first graph shows the "Random Seeds", which are generated

Fig. 3 GUI visualization: (a) starting window of the GUI, (b) additional window in case the "GCODE" option is selected, (c) waiting message at the bottom of the window after pressing the "Generate" button, (d) final windows of the GUI, including the three-dimensional visualization of the pathways and the final message of process completion.

using a custom function to ensure a controlled distribution, and the "Containment Seeds", which are placed along the perimeter to constrain the pattern within the selected area and improve the arrangement of the outer segments. The effect of this constraint is evident in the second graph in Fig. 4a, where a smooth and regular border can be observed.

Fig. 4b and c show a color-coded map representing the area of each Voronoi cell. The same color scheme is applied to the accompanying histogram, which displays the distribution of these area values across the entire pattern. The fiber thickness set by the user is incorporated into this analysis, influencing the calculated porosity by subtracting the area occupied by the fiber from each cell.

The next visualization produced by the software shows the conversion of the pattern into a graph, highlighting its nodes and edges. This is followed by a representation of the continuous path across the structure using a color gradient to indicate the progression along the toolpath (Fig. 4d), which is then used for toolpath generation.

These graphical outputs are stored individually within the folder system and are also collected into a report that includes a summary of the main parameters along with the visualizations described above (Report 1, SI).

The last graphical output is an interactive preview of the actual toolpath, shown separately for each selected printing technique (Fig. 3d). On the left, the MEW toolpath appears as a flat layout with no changes along the Z-axis, as expected for continuous printing. On the right, the FDM path includes visible Z-axis movements, where the extruder lifts to avoid printing twice over the same segments and to prevent contact with already deposited fibers while travelling.

3.2 Voronoi scaffolds

The Voronoi-based pattern generated with the custom software was successfully printed using both the MEW and FDM techniques, as shown in Fig. 5. In both cases, the confocal images confirmed a correct reproduction of the Voronoi layout.

These results confirmed the novelty of the developed platform, as a physiologically relevant and non-repeating pattern is successfully produced by MEW and FDM, overcoming present limitations of software associated with additive manufacturing technologies optimized for regular or parametric geometries.

The scaffolds exhibited a good spatial distribution of the cells and high morphological fidelity in relation to the theoretical pattern, with marginal defects specific for each technique. In particular, the FDM scaffolds presented minor deficits in the connection between a limited number of nodes of the pattern, resulting in the coalescence of a few cells while maintaining the overall backbone structure. Otherwise, the
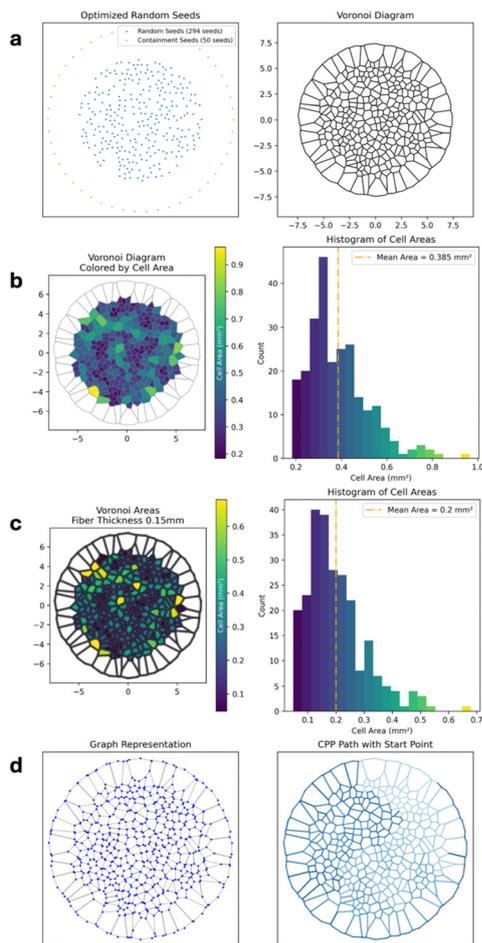
Fig. 4 (a) Visual representation of the generating seeds and the corresponding Voronoi pattern, (b and c) analysis of the pore area, related to input fiber thicknesses of 0 and 0.15 mm, respectively, (d) graph visualization and relative path to travel all the edges.
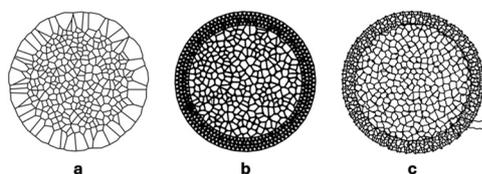

Fig. 5 Theoretical Voronoi architecture (a) and bright-field images of printed structures (FDM (b) and MEW (c)).

MEW scaffold maintained successfully the continuous fiber feature of the process even with such a complex pattern, but losing inevitably some precision in the morphology fidelity, specifically in the shorter segments. Nevertheless, the precision acquired with this technique is reasonably successful, considering the fast and large number of changes of directions implied by the complexity of the pattern.

As expected, the fiber dimension varies between the techniques, with a mean value of 92.01 ± 11.93 μm for the MEW scaffold and 140.96 ± 11.01 μm for the FDM ones. Hence, FDM

achieves precision while limiting the smaller fiber dimensions, whereas MEW is able to reach smaller fibers at the expense of precision.

Notably, the fibre diameters obtained by MEW in this work are slightly larger than those typically reported in the literature. This is primarily related to the geometrical constraints of the printed pattern rather than to intrinsic limitations of the technique. Achieving smaller MEW fibre diameters generally requires long and linear deposition paths to maintain a stable regime above the critical translation speed and to minimize jet lag effects. Given the short segments and frequent changes in direction inherent to the Voronoi architecture, such conditions could not be fully achieved. Nevertheless, the resulting fibre diameters remain smaller than those obtained with the FDM technique.

To test the versatility of the software for different scaffold specifications, several sets of parameters were employed to generate the code and then to print them (Fig. 6).

Moreover, to further evaluate the produced scaffolds, an analysis of the porosity was conducted and compared with the prediction generated by the software.
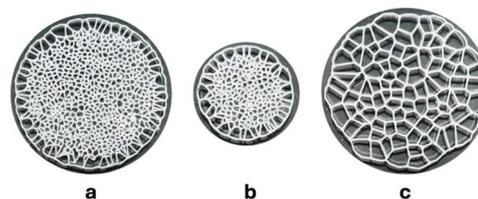

Fig. 6 Validation of the versatility of the software with FDM printing of different pattern parameters: (a) 1200 seeds, a diameter of 14 mm, (b) 650 seeds, a diameter of 7 mm, (c) 100 seeds, a diameter of 14 mm. Images were acquired using an optical imaging system.
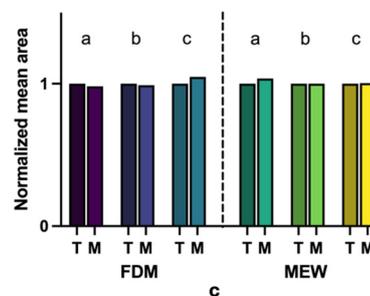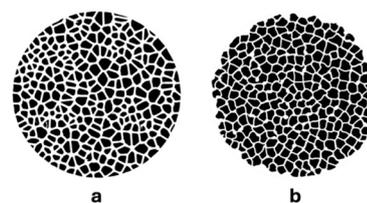

Fig. 7 Porosity evaluation of the printed structures (FDM (a) and MEW (b)) and comparison between the theoretical value (*T*) and the corresponding measured porosity (*M*), normalized to the theoretical area (c).

The results showed good agreement between predicted and experimental values, with an average porosity deviation of 2.2% for the FDM scaffolds and 1.7% for the MEW ones. Specifically, the analysis revealed a mean pore area of 0.213 mm^2 for the FDM scaffolds and 0.270 mm^2 for the MEW scaffolds. These results are consistent with expectations, as the smaller fiber diameter characteristic of the MEW process leads to a reduced material footprint and consequently larger pore areas (Fig. 7).

3.2.1 Complete scaffold characterization. The SEM images acquired from the complete scaffold demonstrated an even distribution of the nanofibers towards the printed Voronoi backbone, highlighting the influence of the microfibers on the space disposition of the electrospun mat. As shown in Fig. 8a,

the nanofibers leaned onto the microfibers following their profile, but within the Voronoi porosities, they extended below the level defined by the microfiber thickness, partially bridging the voids and settling closer to the collector. This resulted in a three-dimensional arrangement of the thin membrane with a slight curvature. Even if the electrospun mat got closer to the collector, it is possible to note in the bottom part of the scaffold (Fig. 8b) that these fibers bridged between a middle plane through the microfiber height. This behaviour is also visible in the images related to the folded scaffold (Fig. 8c and d), where it is possible to appreciate a slight distance between the nanofiber plane and the lower extremity of the microfibers. Moreover, it is possible to note that the nanofibers were able to connect to the Voronoi backbone, forming several anchor-
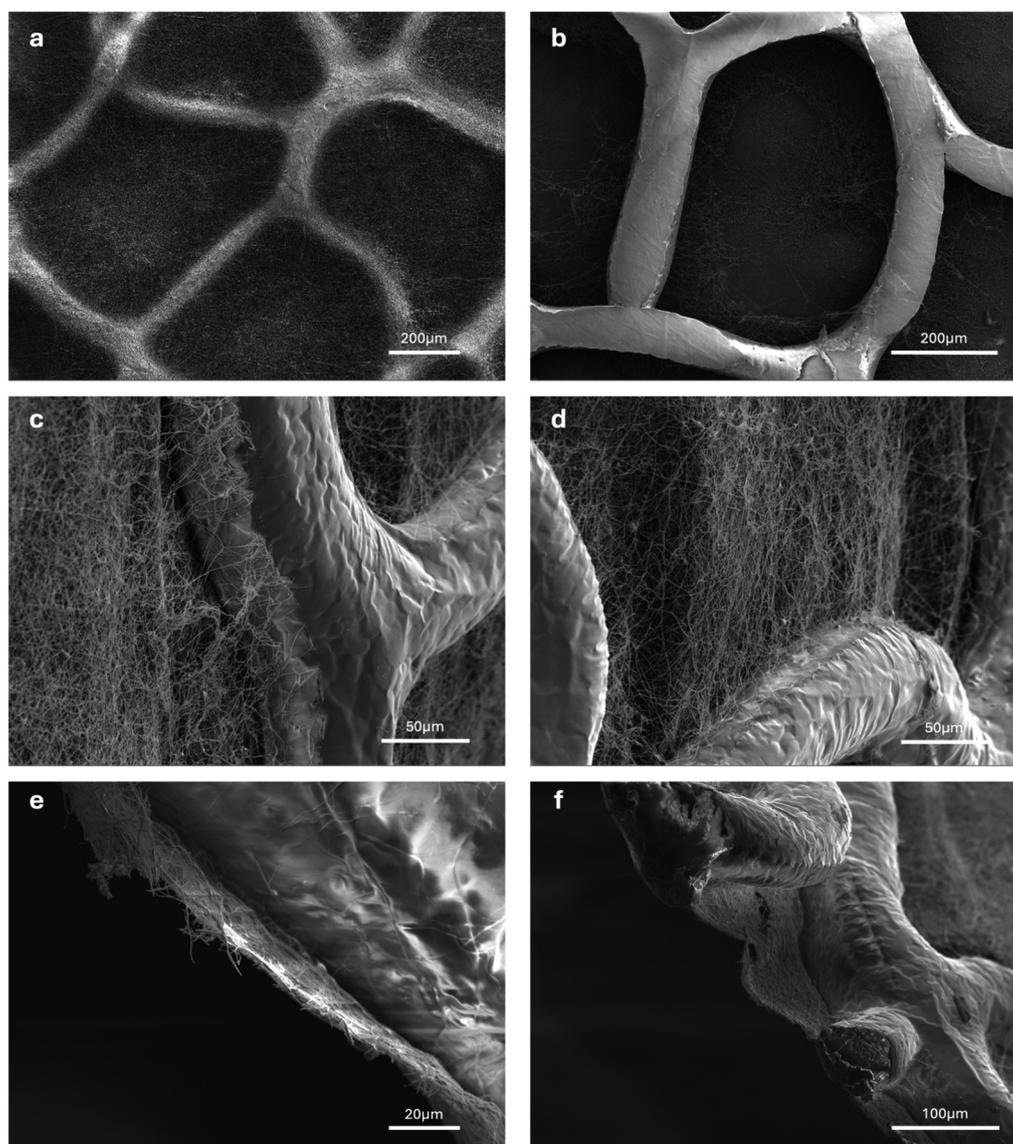

Fig. 8 SEM images of the scaffolds completed with the electrospun membrane: (a) view of the apical side (200X), (b) view of the basolateral side (300X), (c and d) view of the basolateral side in a folded conformation, exposing the interaction between the Voronoi backbone and the nanofibers (1000X), and (e and f) view of the cross section of a sectioned scaffold, showing the membrane thinness (600X).

ing points to the microfibers and efficiently combining the two scaffold components. The two-step approach, proposed for the first time in this work, represents a technological advancement in scaffold production, as it integrates both the biomimetic macro-architecture of tissues and nanofibrous structures of the ECM. Furthermore, it enhances the replication of a physiological environment, which is fundamental to the advancement of *in vitro* tissue and organ development.[61] Lastly, to evaluate the membrane thickness, scaffolds were sectioned to observe the cross-section (Fig. 8e and f). The analysis revealed an average thickness of 3 μm, confirming the production of an ultra-thin membrane integrated inside the 3D-printed structure.

3.3 *In vitro* cell culture characterization

The developed scaffolds proved to support the adhesion and proliferation of both cell types on each side of the construct, enabling the formation of a functional barrier. The electrospun membrane, previously optimized by Licciardello *et al.*,[43] proved effective in supporting epithelial cell attachment while ensuring sufficient nutrient exchange across the membrane, as demonstrated by the successful establishment of the ALI condition started from day 3. Immunofluorescence staining, performed at the end of the culture (day 10), confirmed the selec-

tive colonization of the two cellular compartments. A549 epithelial cells showed high proliferation on the apical side of the membrane, while HUVECs successfully adhered and spread on the basolateral side following seeding on day 7.

The thinness of the electrospun membrane was confirmed by the possibility of simultaneously visualizing both cell layers during confocal imaging, as visible in SI videos (video S1 and video S2), where the DAPI/phalloidin staining relative to A549 is visible from the basolateral side. This optical transparency suggests a membrane thinness that likely enhances cellular crosstalk across the membrane, offering higher biomimicry than conventional models that use thicker[39,62,63] membranes (10–25 μm).

Confocal images further highlighted the influence of the microfilament structure on the 3D organization of the cells on the apical side. As shown in Fig. 9(b and e), darker regions can be observed in correspondence with the microfiber locations. This effect is due to the fact that cells adhering to the fibers are positioned at a different focal plane compared to those growing on the membrane, which occupies the larger area of the Voronoi pores.

As a result, when averaging the Z-stack signal, the contribution of out-of-focus cells on the fibers is reduced, generating shadow-like regions that indirectly highlight the presence and
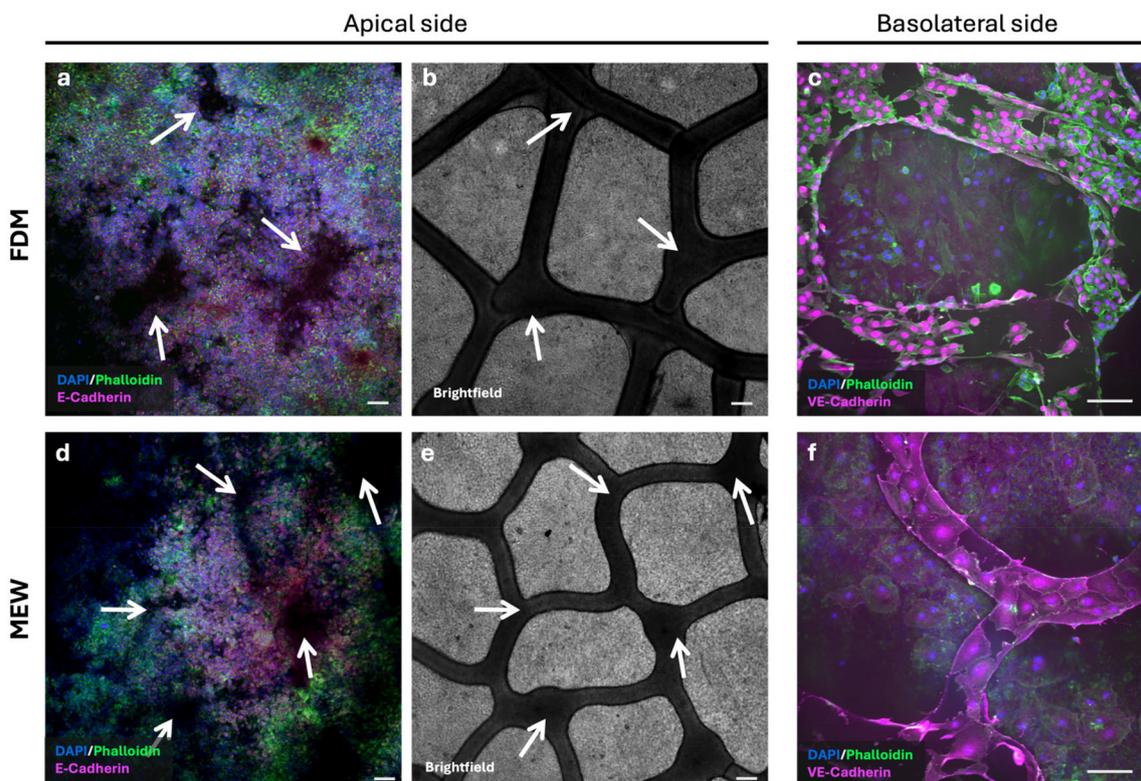

Fig. 9 Biological characterization of the models produced both with FDM and MEW. (a and d) Immunofluorescence confocal microscopy images of the apical side of the scaffolds; shadows caused by the three-dimensional disposition of the membrane on the microfibers are highlighted with arrows. (b and e) Bright-field confocal microscopy images to visualize the 3D-printed fibers and the relative position of the arrows on the Voronoi backbone. (c and f) Immunofluorescence confocal microscopy images of the basolateral side of the scaffolds, exposing the endothelial cells interacting both with the microfibers and with the electrospun mat. Scale bars: 100 μm.

spatial impact of the printed backbone. On the basolateral side, where HUVECs were exposed to both the membrane and the microfibers, cells were found to colonize both components (Fig. 9c, f and SI video S3). Notably, HUVECs displayed a more spread morphology on the electrospun mat as well as on MEW microfibers. However, non-cuboidal morphologies were observed on FDM filaments, where HUVECs adopted more clustered shapes along the fibers, suggesting that fiber size and topology could affect the spatial adaptation of endothelial cells.

Overall, this work introduces an alveolar-capillary barrier model offering several contributions. First, it provides more biomimetic confinement of cells within smaller alveolus-like compartments compared to the flat membranes used with transwell inserts[43,64–67] and lung-on-chip.[68–72] In addition, in contrast to other approaches relying on regular pore arrangements such as hexagonal lattices[28] or inverse opal scaffolds,[73] the developed constructs use a complex Voronoi-inspired pattern that more closely reflects the heterogeneous geometry of the alveolar septa. To our knowledge, this degree of biomimicry has not been previously employed in the context of *in vitro* alveolar modelling. Furthermore, the strategy proved to be technically versatile, being successfully applied to both MEW and FDM scaffolds, thus not relying on a single fabrication technique. However, it should be noted that the pore dimensions obtained in this study are not yet at the physiological alveolar scale, and the present model should therefore be considered a first step toward more refined biomimetic constructs.

4 Conclusions

A novel strategy for the development of alveolar *in vitro* models was presented, combining bioinspired design, custom fabrication tools, and hybrid manufacturing approaches.

A two-dimensional Voronoi pattern was employed to generate a biomimetic scaffold layout, aiming to replicate the irregular yet optimized geometry of the native alveolar tissue. To enable the physical fabrication of such a complex and nonrepeating geometry, custom Python-based software was developed to generate continuous extrusion paths optimized for both melt electrowriting (MEW) and fused deposition modelling (FDM). By implementing principles of graph theory, the tool was able to minimize non-productive movements while maintaining full control over extruder trajectories. Moreover, the introduction of a porosity predictive tool established a direct link between design parameters and scaffold properties, thereby reducing the trial-and-error process typically required in scaffold optimization.

The printed Voronoi backbone was integrated with an electrospun nanofibrous membrane, providing a multiscale construct that combines the morphological fidelity of additive manufacturing with the ECM-like features of electrospinning. This combination allowed the fabrication of ultrathin membranes that, thanks to the mechanical support provided by the printed frame, could be easily handled and assembled without compromising structural integrity.

Biological evaluation demonstrated the suitability of the scaffold for supporting co-cultures of epithelial and endothelial cells seeded on opposite sides of the membrane. The construct successfully reproduced a compartmentalized barrier structure and allowed cell proliferation and organization across both sides, indicating its potential as a physiologically relevant alveolar barrier model.

This work relies on the established literature demonstrating that the scaffold architecture, such as the difference between aligned and random fibers and the effect of curved or nonlinear geometries, can influence cell arrangement and collective cellular responses within engineered tissues. In this context, increasing architectural biomimicry is widely regarded as a promising strategy to improve the physiological relevance of *in vitro* models. Hence, the Voronoi-inspired design presented here follows this rationale by introducing a controlled irregular geometry that more closely reflects native tissue organization. While the present study primarily demonstrates feasibility and biological compatibility, it represents an initial step toward investigating how architectural biomimicry may contribute to enhanced tissue functionality. Overall, the proposed strategy represents a promising step forward in the design and fabrication of complex biomimetic systems for tissue modelling by combining ad hoc generated software to reassemble Voronoi-like physiological architectures with multimaterial and multi-process technological approaches.

Conflicts of interest

There are no conflicts to declare.

Data availability

All the data are available within the manuscript and in the supplementary information (SI). Supplementary information: Video S1: Z-stack cellularized FDM scaffold; Video S2: Z-stack cellularized MEW scaffold; Video S3: 3D projection cellularized FDM scaffold; File S4: Report example produced by the software. See DOI: https://doi.org/10.1039/d5bm01834j.

The script of the software is available at https://github.com/BioinsideLab/PyVoroGen—Voronoi-Path-Generator.

Acknowledgements

References

1 P. Makvandi, A. Maleki, M. Shabani, A. R. Hutton, M. Kirkby, R. Jamaledin, T. Fang, J. He, J. Lee, B. Mazzolai, R. F. Donnelly, F. R. Tay, G. Chen and V. Mattoli, *Matter*, 2022, **5**, 390–429.

2 A. J. Koch and H. Meinhardt, *Rev. Mod. Phys.*, 1994, **66**, 1481–1507.

3 X. Wei, Y. Wang, Y. Liu, K. Ji, K. Li, J. Wang and Z. Gu, *Matter*, 2024, **7**, 826–854.

4 J. Adhikari, A. Roy, A. Chanda, G. D. A. S. Thomas, M. Ghosh, J. Kim and P. Saha, *Biomater. Sci.*, 2023, **11**, 1236–1269.

5 S. Kim, J. J. Cassidy, B. Yang, R. W. Carthew and S. Hilgenfeldt, *Biophys. J.*, 2016, **111**, 2735–2746.

6 V. Perricone, T. B. Grun, F. Rendina, F. Marmo, M. D. Candia Carnevali, M. Kowalewski, A. Facchini, M. De Stefano, L. Santella, C. Langella and A. Micheletti, *J. R. Soc., Interface*, 2022, **19**, 20220226.

7 H. Togashi, S. R. Davis and M. Sato, *Dev. Biol.*, 2024, **506**, 1–6.

8 T. Xu and M. Li, *Philos. Mag.*, 2009, **89**, 349–374.

9 A. K. Arvizu Alonso, E. N. Armendáriz Mireles, C. A. Calles Ariaga and E. Rocha Rangel, *Designs*, 2024, **8**, 93.

10 D. L. González and T. L. Einstein, *Phys. Rev. E:Stat., Nonlinear, Soft Matter Phys.*, 2011, **84**, 051135.

11 A. Q. Nguyen, J. Huang and D. Bi, *Nat. Commun.*, 2025, **16**, 3260.

12 D. Bi, X. Yang, M. C. Marchetti and M. L. Manning, *Phys. Rev. X*, 2016, **6**, 021011.

13 C. Lau, B. Kalantari, K. P. Batts, L. D. Ferrell, S. L. Nyberg, R. P. Graham and R. K. Moreira, *Sci. Rep.*, 2021, **11**, 9343.

14 H. Chen, Y. Liu, C. Wang, A. Zhang, B. Chen, Q. Han and J. Wang, *Comput. Biol. Med.*, 2021, **130**, 104241.

15 H. Zhao, Y. Han, C. Pan, D. Yang, H. Wang, T. Wang, X. Zeng and P. Su, *Micromachines*, 2021, **12**, 664.

16 Y. Zhou, P. Isaksson and C. Persson, *J. Mech. Behav. Biomed. Mater.*, 2023, **148**, 106172.

17 J. Deering, K. I. Dowling, L.-A. DiCecco, G. D. McLean, B. Yu and K. Grandfield, *J. Mech. Behav. Biomed. Mater.*, 2021, **116**, 104361.

18 H. Wu, L. Chao, Q. Zhang, Y. Yi, C. Jiao, Y. Ye, L. Shen, J. Zhao, G. Wu and C. Wang, *Mater. Today Commun.*, 2022, **33**, 104559.

19 D. McCoul, W. Nie, P. Kim, C. Kengla, C. Clouse and A. Atala, *Bioprinting*, 2022, **28**, e00252.

20 M. Laubach, B. Herath, N. Bock, S. Suresh, S. Saifzadeh, B. L. Dargaville, J. McGovern, M.-L. Wille, D. W. Hutmacher and F. Medeiros Savi, *Front. Bioeng. Biotechnol.*, 2023, **11**, 1272348.

21 Y. Wang, Z. Wu, C. Ma, J. Chen, Y. Wu, D. Gao, L. Chen and H. Wang, *Mater. Technol.*, 2025, **40**, 2481637.

22 H. Liang, Y. Yang, D. Xie, L. Li, N. Mao, C. Wang, Z. Tian, Q. Jiang and L. Shen, *J. Mater. Sci. Technol.*, 2019, **35**, 1284–1297.

23 G. Beltrán, D. Navajas and J. M. García-Aznar, *J. Mech. Behav. Biomed. Mater.*, 2022, **126**, 105043.

24 A. Ishikawa and K. Koshiyama, *Respir. Physiol. Neurobiol.*, 2022, **302**, 103900.

25 K. Koshiyama and S. Wada, *Comput. Biol. Med.*, 2015, **62**, 25–32.

26 A. E. Medvedev, V. M. Fomin and P. S. Gafurova, *J. Appl. Mech. Tech. Phys.*, 2020, **61**, 1–13.

27 D. Baptista, L. M. Teixeira, Z. T. Birgani, S. Van Riet, T. Pasman, A. Poot, D. Stamatialis, R. Rottier, P. Hiemstra, P. Habibović, C. Van Blitterswijk, S. Giselbrecht and R. Truckenmüller, *Biomaterials*, 2021, **266**, 120436.

28 P. Zamprogno, S. Wüthrich, S. Achenbach, G. Thoma, J. D. Stucki, N. Hobi, N. Schneider-Daum, C.-M. Lehr, H. Huwer, T. Geiser, R. A. Schmid and O. T. Guenat, *Commun. Biol.*, 2021, **4**, 168.

29 G. Lovric, R. Mokso, F. Arcadu, I. Vogiatzis Oikonomidis, J. C. Schittny, M. Roth-Kleiner and M. Stampanoni, *Sci. Rep.*, 2017, **7**, 12545.

30 S. Gómez, M. Vlad, J. López and E. Fernández, *Acta Biomater.*, 2016, **42**, 341–350.

31 B. L. Devlin, M. C. Allenby, J. Ren, E. Pickering, T. J. Klein, N. C. Paxton and M. A. Woodruff, *Adv. Funct. Mater.*, 2024, **34**, 2313092.

32 K. L. O'Neill and P. D. Dalton, *Small Methods*, 2023, **7**, 2201589.

33 J. Ren, R. Murray, C. S. Wong, J. Qin, M. Chen, M. Totsika, A. D. Riddell, A. Warwick, N. Rukin and M. A. Woodruff, *Polymers*, 2022, **14**, 763.

34 R. Sanchez Diaz, J. Park, L. L. Rodrigues, P. D. Dalton, E. M. De-Juan-Pardo and T. R. Dargaville, *Adv. Mater. Technol.*, 2022, **7**, 2100508.

35 P. G. Saiz, A. Reizabal, J. L. Vilas-Vilela, P. D. Dalton and S. Lanceros-Mendez, *Adv. Mater.*, 2024, **36**, 2312084.

36 C. G. Kim, K. S. Han, S. Lee, M. C. Kim, S. Y. Kim and J. Nah, *Appl. Sci.*, 2021, **11**, 6351.

37 Y. Han, H. Wang, Y. Guan, S. Li, Z. Yuan, L. Lu and X. Zheng, *Biomed. Mater.*, 2024, **19**, 035042.

38 R. Winarso, P. Anggoro, R. Ismail, J. Jamari and A. Bayuseno, *Heliyon*, 2022, **8**, e11701.

39 D. Cei, A. Doryab, A. Lenz, A. Schröppel, P. Mayer, G. Burgstaller, R. Nossa, A. Ahluwalia and O. Schmid, *Biotechnol. Bioeng.*, 2021, **118**, 690–702.

40 R. S. Murkar, C. Wiese-Rischke, T. Weigel, S. Kopp and H. Walles, *J. Tissue Eng.*, 2025, **16**, 20417314241299076.

41 P. Jain, A. Nishiguchi, G. Linz, M. Wessling, A. Ludwig, R. Rossaint, M. Möller and S. Singh, *Adv. Biol.*, 2021, **5**, 2000427.

42 P. Jain, S. B. Rauer, D. Felder, J. Linkhorst, M. Möller, M. Wessling and S. Singh, *ACS Biomater. Sci. Eng.*, 2023, **9**, 4878–4892.

43 M. Licciardello, V. Sgarminato, G. Ciardelli and C. Tonda-Turo, *Biomater. Adv.*, 2023, **154**, 213620.

44 S. Giannitelli, P. Mozetic, M. Trombetta and A. Rainer, *Acta Biomater.*, 2015, **24**, 1–11.

45 N. W. Pensa, A. S. Curry, P. P. Bonvallet, N. F. Bellis, K. M. Rettig, M. S. Reddy, A. W. Eberhardt and S. L. Bellis, *Biomater. Res.*, 2019, **23**, 22.

46 Q. Gao, P. Zhao, R. Zhou, P. Wang, J. Fu and Y. He, *Bio-Des. Manuf.*, 2019, **2**, 1–9.

47 P. Ginestra, S. Pandini and E. Ceretti, *Rapid Prototyp. J.*, 2019, **26**, 593–602.

48 W. King and G. Bowlin, *Polymers*, 2021, **13**, 1097.

49 S. H. Park, T. G. Kim, H. C. Kim, D.-Y. Yang and T. G. Park, *Acta Biomater.*, 2008, **4**, 1198–1207.

50 T. Jungst, I. Pennings, M. Schmitz, A. J. W. P. Rosenberg, J. Groll and D. Gawlitta, *Adv. Funct. Mater.*, 2019, **29**, 1905987.

51 K. F. Eichholz, P. Pitacco, R. Burdis, F. Chariyev-Prinz, X. Barceló, B. Tornifoglio, R. Paetzold, O. Garcia and D. J. Kelly, *Adv. Healthcare Mater.*, 2024, **13**, 2302057.

52 K. M. A. Mueller, A. Hangleiter, S. Burkhardt, D. M. Rojas-González, C. Kwade, S. T. Pammer, S. Leonhardt and P. Mela, *Small Sci.*, 2023, **3**, 2300021.

53 X. Zhou, Y. Qian, L. Chen, T. Li, X. Sun, X. Ma, J. Wang and C. He, *ACS Nano*, 2023, **17**, 5140–5156.

54 E. Rezvani Ghomi, V. Chellappan, R. E. Neisiany, N. Dubey, K. Amuthavalli, N. K. Verma, R. Lakshminarayanan and S. Ramakrishna, *Compos. Sci. Technol.*, 2024, **247**, 110402.

55 M. Yeo and G. Kim, *Acta Biomater.*, 2020, **107**, 102–114.

56 A. Nandakumar, A. Barradas, J. De Boer, L. Moroni, C. Van Blitterswijk and P. Habibovic, *Biomatter*, 2013, **3**, e23705.

57 P. Romero-Araya, V. Pino, A. Nenen, V. Cárdenas, F. Pavicic, P. Ehrenfeld, G. Serandour, J. G. Lisoni, I. Moreno-Villoslada and M. E. Flores, *Polymers*, 2021, **13**, 3806.

58 A. Gleadall, *Addit. Manuf.*, 2021, **46**, 102109.

59 M. Licciardello, C. Traldi, M. Cicolini, V. Bertana, S. L. Marasso, M. Cocuzza, C. Tonda-Turo and G. Ciardelli, *Front. Bioeng. Biotechnol.*, 2024, **12**, 1346660.

60 C. Tonda-Turo, E. Cipriani, S. Gnavi, V. Chiono, C. Mattu, P. Gentile, I. Perroteau, M. Zanetti and G. Ciardelli, *Mater. Sci. Eng., C*, 2013, **33**, 2723–2735.

61 K. J. Juarez-Navarro, V. Guarino and M. A. Alvarez-Perez, *Fibers*, 2025, **13**, 83.

62 W. She, C. Shen, Y. Ying and Q. Meng, *Lab Chip*, 2024, **24**, 85–96.

63 D. Huh, B. D. Matthews, A. Mammoto, M. Montoya-Zavala, H. Y. Hsin and D. E. Ingber, *Science*, 2010, **328**, 1662–1668.

64 J. R. Grunwell, S. T. Stephenson, G. A. Dallalio, B. A. Diani, C. Zaworski, N. Jordan and A. M. Fitzpatrick, *Sci. Rep.*, 2025, **15**, 17703.

65 P. Jain, A. Nishiguchi, G. Linz, M. Wessling, A. Ludwig, R. Rossaint, M. Möller and S. Singh, *Adv. Biol.*, 2021, **5**, 2000427.

66 R. S. Murkar, C. Wiese-Rischke, T. Weigel, S. Kopp and H. Walles, *J. Tissue Eng.*, 2025, **16**, 20417314241299076.

67 S. Van Riet, D. K. Ninaber, H. M. M. Mikkers, T. D. Tetley, C. R. Jost, A. A. Mulder, T. Pasman, D. Baptista, A. A. Poot, R. Truckenmüller, C. L. Mummery, C. Freund, R. J. Rottier and P. S. Hiemstra, *Sci. Rep.*, 2020, **10**, 5499.

68 A. O. Stucki, J. D. Stucki, S. R. R. Hall, M. Felder, Y. Mermoud, R. A. Schmid, T. Geiser and O. T. Guenat, *Lab Chip*, 2015, **15**, 1302–1310.

69 A. Doryab, M. B. Taskin, P. Stahlhut, A. Schröppel, D. E. Wagner, J. Groll and O. Schmid, *Adv. Funct. Mater.*, 2021, **31**, 2004707.

70 M. Guan, S. Tang, H. Chang, Y. Chen, F. Chen, Y. Mu, D. Zhao, W. Fan, H. Tian, D. C. Darland and Y. Zhang, *Ecotoxicol. Environ. Saf.*, 2021, **223**, 112601.

71 P. Jain, S. B. Rauer, D. Felder, J. Linkhorst, M. Möller, M. Wessling and S. Singh, *ACS Biomater. Sci. Eng.*, 2023, **9**, 4878–4892.

72 D. Huh, B. D. Matthews, A. Mammoto, M. Montoya-Zavala, H. Y. Hsin and D. E. Ingber, *Science*, 2010, **328**, 1662–1668.

73 L. Lü, H. Shen, D. Kasai and Y. Yang, *Stem Cells Int.*, 2022, **2022**, 1–12.